ACS NANO
Cite This: ACS Nano 2019, 13, 7527−7535
www.acsnano.org

ARTICLE

Continuous Heteroepitaxy of Two-Dimensional Heterostructures Based on Layered Chalcogenides

Yu Kobayashi,[†] Shoji Yoshida,[‡] Mina Maruyama,[‡] Hiroyuki Mogi,[‡] Kota Murase,[‡] Yutaka Maniwa,[†] Osamu Takeuchi,[‡] Susumu Okada,[‡] Hidemi Shigekawa,[‡] and Yasumitsu Miyata*,[†]

[†]Department of Physics, Tokyo Metropolitan University, Hachioji, Tokyo 192-0397, Japan
[‡]Faculty of Pure and Applied Sciences, University of Tsukuba, Tsukuba 305-8573, Japan

Supporting Information

Downloaded via UNIV OF TSUKUBA on October 21, 2019 at 01:45:02 (UTC).
See https://pubs.acs.org/sharingguidelines for options on how to legitimately share published articles.

ABSTRACT: **The in-plane connection and layer-by-layer stacking of atomically thin layered materials are expected to allow the fabrication of two-dimensional (2D) heterostructures with exotic physical properties and future engineering applications. However, it is currently necessary to develop a continuous growth process that allows the assembly of a wide variety of atomic layers without interface degradation, contamination, and/or alloying. Herein, we report the continuous heteroepitaxial growth of 2D multiheterostructures and nanoribbons based on layered transition metal dichalcogenide (TMDC) monolayers, employing metal organic liquid precursors with high supply controllability. This versatile process can avoid air exposure during growth process and enables the formation of in-plane heterostructures with ultraclean atomically sharp and zigzag-edge straight junctions without defects or alloy formation around the interface. For the samples grown directly on graphite, we have investigated the local electronic density of states of atomically sharp heterointerface by scanning tunneling microscopy and spectroscopy, together with first-principles calculations. These results demonstrate an approach to realizing diverse nanostructures such as atomic layer-based quantum wires and superlattices and suggest advanced applications in the fields of electronics and optoelectronics.**

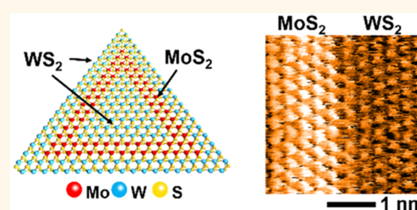

KEYWORDS: *transition metal dichalcogenides, two-dimensional materials, semiconductor, heterostructures, chemical vapor deposition*

Heteroepitaxial growth is widely used to fabricate thin films of conventional solid materials on substrates. During this process, the crystal orientation of the film can be controlled based on the orientation of the substrate. This technique also enables the formation of highly crystalline heterointerfaces,[1] various semiconductor quantum well structures,[2−4] and superlattice structures.[5,6] All these are important in modern condensed matter physics and have applications in electronics and optoelectronics.[7−10] Recently, similar epitaxial growth processes and the resulting heterostructures have been realized with atomically thin layers of so-called two-dimensional (2D) materials, including graphene, hexagonal boron nitride (hBN), and transition metal dichalcogenides (TMDCs).[11−23] In such cases, epitaxial growth can be initiated at the edges of the 2D material, resulting in the formation of an in-plane 2D heterostructure with a one-dimensional interface. These 2D heterostructures have attracted much attention as promising systems that allow the investigation of low-dimensional quantum phenomena and may also lead to the development of high-performance devices.

TMDC atomic layers are ideal materials for the fabrication of functional 2D heterostructures because they exhibit composition-dependent tunable electronic properties and intriguing spin-valley physics.[24−28] In previous studies, TMDC growth has been primarily obtained using vapor-phase deposition with solid precursors such as metal oxides and chalcogens.[14−17] These solid precursors typically have low vapor pressures at room temperature and thus require high temperatures (often above 600 °C) for vaporization. In the early studies, this requirement frequently makes it difficult to repeatedly supply different precursors while maintaining a controlled growth rate during epitaxial growth. To solve this issue, several approaches have been recently reported to control precursor supply rates and to realize multiheterojunctions.[20,21,23] For example, Zhang et al. have achieved the sequential vapor deposition of solid precursors of various multiheterostructures of MoS_2, $MoSe_2$, WS_2, and WSe_2 using a reverse flow.[20] In this case, the regrowth is conducted with a separate vapor deposition system and the continuous growth has never been demonstrated. Similar multiheterostructures

Received: October 19, 2018
Accepted: May 31, 2019
Published: May 31, 2019

© 2019 American Chemical Society

DOI: 10.1021/acsnano.8b07991
ACS Nano 2019, 13, 7527−7535

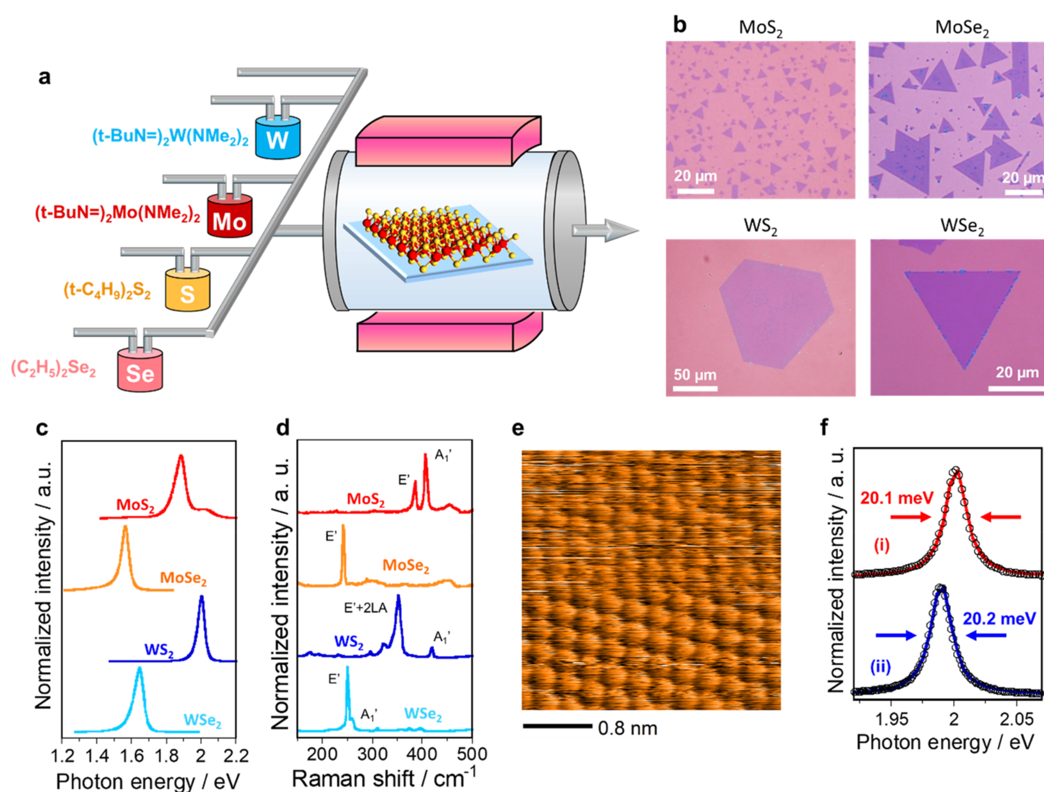

Figure 1. (a) Schematic illustration of the present MOCVD system. (b) Optical microscopy images, (c) PL spectra, and (d) Raman spectra of monolayers composed of MoS_2, $MoSe_2$, WS_2, and WSe_2 grains. (e) High-resolution STM image of a MoS_2 monolayer grown on graphite, acquired using the settings V_s = +2.0 V and I_t = 0.1 nA, where V_s and I_t are the sample voltage and tunneling current, respectively. (f) PL spectra of WS_2 monolayers grown on graphite using (i) liquid precursors at 640 °C (red) and (ii) WO_3 and S at 1100 °C (blue).

based on MoS_2/WS_2 and $MoSe_2/WSe_2$ have been continuously grown by water-assisted supply control of solid metal precursors.[21] Instead of such solid precursors, organic metal/chalcogen precursors with high vapor pressure have been also used to fabricate the multiheterostructures.[23] For these organic precursors, the heterostructures are prepared with the precise flow control of all metal and chalcogen precursors without air exposure. Even though there has been such outstanding progress, it still remains necessary to develop a sophisticated technique for forming 2D heterostructures with an atomically straight interface and to characterize their interface atomic/electronic structures.

In the present work, we demonstrated a versatile, repeatable method for the heteroepitaxial growth of 2D multiheterostructures and semiconductor nanoribbon structures, based on using liquid precursors. TMDC growth was performed with a lab-made metal organic chemical vapor deposition (MOCVD) system in conjunction with liquid organic metal and chalcogen precursors, as shown in Figure 1a. Using this system, we were able to grow four different types of atomic TMDC layers, consisting of WS_2, WSe_2, MoS_2, and $MoSe_2$ monolayers. The heteroepitaxial growth of these monolayers allowed the fabrication of multiheterostructures, as well as nanoribbon structures 20 nm wide and with six different TMDC-based semiconductor heterostructures. We have investigated the local electronic density of states of atomically sharp heterointerface by scanning tunneling microscopy (STM) and spectroscopy (STS), together with first-principles calculations. Fine tuning of the growth rates enabled the formation of atomically straight interfaces with perfect metal zigzag edges in MoS_2/WS_2 heterostructures. These high-quality interfaces were employed to elucidate the band diagram of the type I straddling gap at the heterointerface.

RESULTS AND DISCUSSION

The liquid precursors used in this work were found to permit the rapid growth of high-quality TMDC monolayer single crystals having wide areas at low temperature under atmospheric pressure. As shown in the optical microscopy images provided in Figure 1b, MoS_2, $MoSe_2$, WS_2, and WSe_2 monolayers were grown on SiO_2/Si substrates under optimized conditions. These monolayer grains generally exhibited typical 3-fold symmetry with straight edges, indicating the preferential formation of metal zigzag edges.[29] These grains also showed the expected photoluminescence (PL) and Raman peaks (Figure 1c,d). We note that the use of alkali metal halides as growth promotors was critical to increasing the crystal size and quality (Figure S1). Similar results have been observed in prior work using different precursors.[22,23,30−32] This could be derived from the formation of intermediate products of alkali metals and transition metals, and the details will be reported elsewhere. Both grain size and quality were also affected by the rate at which the metal and chalcogen precursors were supplied (Figure S2). The STM image provided evidence for highly crystalline lattices in the TMDC monolayers (Figure 1e). The quality of each sample could also be confirmed based on the narrow full-width at half-maximum (fwhm) values of the PL peaks. It has been previously reported that the PL line widths become much narrower when the samples are grown on graphite substrates.[33] As an example, the PL peak generated by the WS_2 monolayer on graphite had an fwhm value of 20 meV and could be fitted by a single Lorentzian function (Figure 1f).

DOI: 10.1021/acsnano.8b07991
ACS Nano 2019, 13, 7527−7535

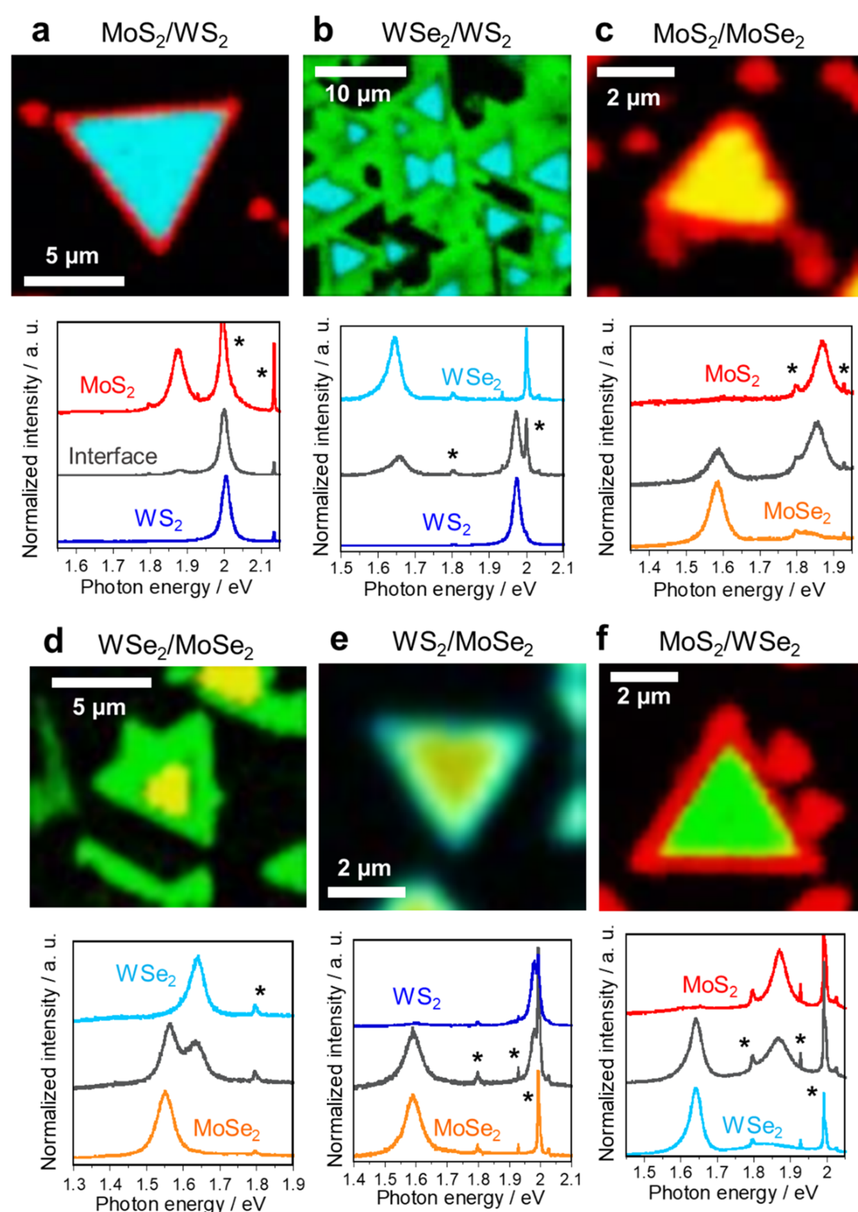

Figure 2. PL intensity maps and PL spectra of (a) MoS_2/WS_2, (b) WSe_2/WS_2, (c) $MoS_2/MoSe_2$, (d) $WSe_2/MoSe_2$, (e) $WS_2/MoSe_2$, and (f) MoS_2/WSe_2 single heterostructures. In the PL intensity maps, red, yellow, cyan, and green correspond to the intensities of the MoS_2, $MoSe_2$, WS_2, and WSe_2 peaks, respectively. Sharp peaks indicated by asterisks correspond to the Raman modes of the graphite substrate.

A similar narrow line width has been observed for the high quality monolayer WS_2 grown on graphite with solid precursors at 1100 °C.[33] Overall, these results indicate that the present method can produce high-quality samples with reduced quantities of structural defects and charged impurities even at a low temperature of 640 °C and under atmospheric pressure.

The heteroepitaxial growth of these monolayers produced six different in-plane heterostructures. Figures 2 and S3 display the PL intensity maps, PL spectra, optical images, and Raman spectra of MoS_2/WS_2, WSe_2/WS_2, $MoS_2/MoSe_2$, $WSe_2/MoSe_2$, $WS_2/MoSe_2$, and MoS_2/WSe_2 monolayers grown on graphite used as a substrate to allow for STM observations. In each spectrum, PL peaks attributable to the inner and outer TMDCs can be clearly seen. This result indicates that the initially grown grains were able to maintain their structure and composition during the second growth step, as a result of the high degree of crystallinity of the initial grains. In almost every sample, the second-growth TMDCs were preferentially formed around the edges of the first-growth grains rather than on the surface. It is therefore evident that the edges were the most active sites in terms of incorporating diffusing atoms under the present conditions.

The edge-initiated heteroepitaxial growth observed in this work would be advantageous when fabricating multiheterostructures and nanoribbon structures. As a demonstration, we prepared a multiheterostructure having a $WS_2/MoS_2/WS_2$ structure by varying the precursors, as shown in Figure 3a–f. The optical microscopy image and PL maps/spectra clearly demonstrated that an MoS_2 monolayer was sandwiched between inner and outer WS_2 monolayers within a single triangular grain. Furthermore, the growth rate could be tuned by adjusting the flow rate of the gas used to transport the liquid precursors, thus enabling control of the size of the epitaxially

DOI: 10.1021/acsnano.8b07991
ACS Nano 2019, 13, 7527−7535

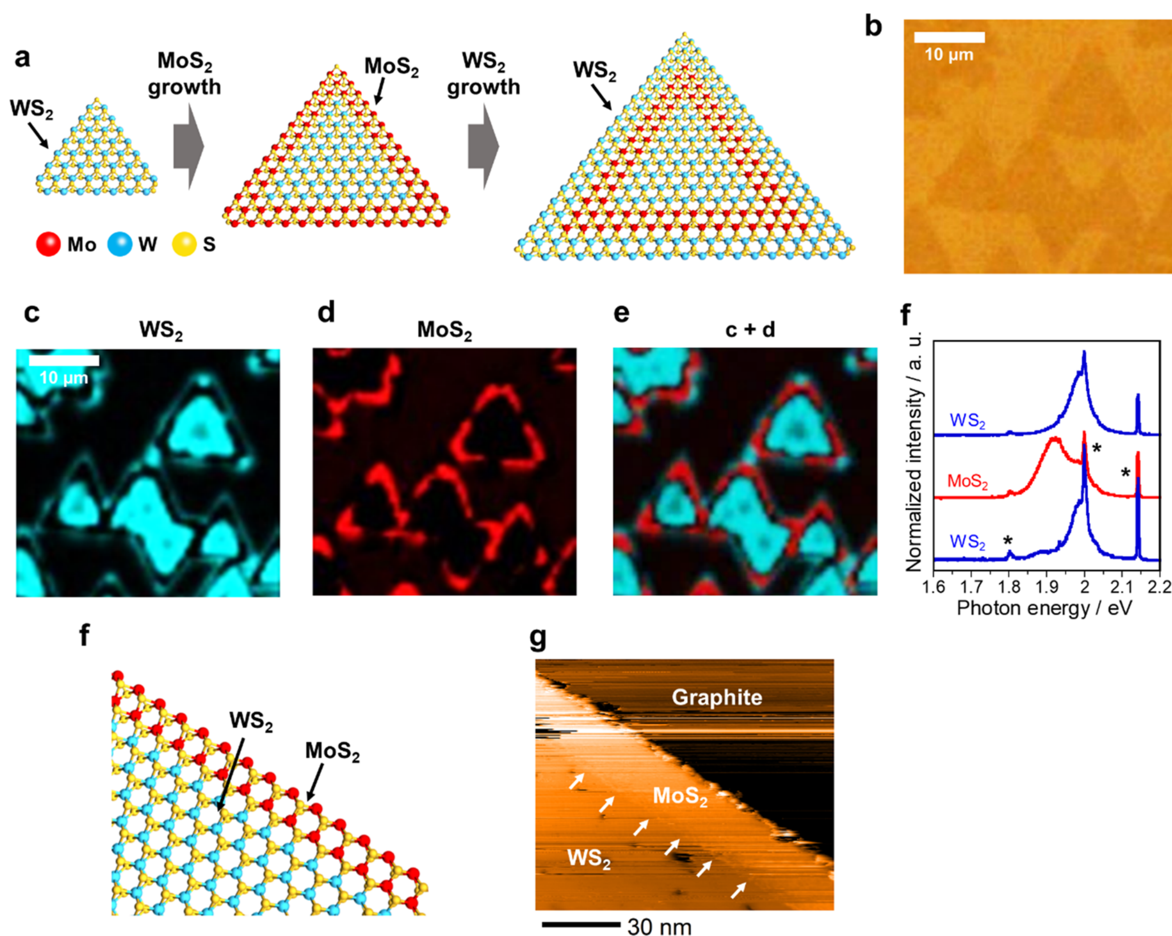

Figure 3. (a) Schematic illustrations of the heteroepitaxial growth of a $WS_2/MoS_2/WS_2$ in-plane multiheterostructure. (b−f) Optical microscopy image, PL intensity maps, and PL spectra of a $WS_2/MoS_2/WS_2$ in-plane multiheterostructure. In the PL intensity maps, red and cyan correspond to the intensities of the MoS_2 and WS_2 PL peaks, respectively. Sharp peaks indicated by asterisks correspond to the Raman modes of the graphite substrate. (g) Schematic illustration and (h) STM image (V_s = +1.0 V, I_t = 0.05 nA) of a MoS_2 monolayer nanoribbon grown from the edge of a WS_2 monolayer. The white arrows indicate the MoS_2/WS_2 heterointerface.

grown TMDC grains. This same process could also be used to produce nanoribbon structures consisting of TMDC monolayers. In the present study, WS_2 grains were initially synthesized, after which MoS_2 monolayers were grown around these earlier grains, applying a slow growth rate, as illustrated in Figure 3g. This process resulted in the formation of nanoribbon structures made of MoS_2 monolayers, having widths of 20 nm, as shown in the STM image in Figure 3h. Here, the white arrows indicate the MoS_2/WS_2 heterointerface. In this image, the difference in contrast between the MoS_2 and the WS_2 regions is derived from their local density of state (LDOS) values.[15,34] This nanoribbon could have a zigzag edge, as discussed further on.

In addition to in-plane heterostructures, vertically stacked heterostructures based on TMDCs could be produced using the same system. As shown in Figure 4a, a second growth TMDC layer was applied to the surface of an initial monolayer. During these trials, we found that the nucleation density at the TMDC surface could be enhanced by cooling the substrate to room temperature before the second growth. In the case of the growth of WSe_2 on a first-growth WS_2 monolayer on graphite, STM observations revealed that small triangular WSe_2 grains were formed on the WS_2 surface and that these grains had two primary orientations (Figure 4b). This result clearly demonstrates that the crystal orientation of the WSe_2 monolayer reflected the crystal lattice of the underlying WS_2, suggesting the van der Waals heteroepitaxial growth of the WSe_2 on the WS_2. In addition, the grains exhibited a distinct moiré pattern in the triangular lattice, as expected for a lattice-mismatched vertical heterostructure such as that in Figure 4c. The period of each moiré pattern was approximately 8.2 nm, which is consistent with the difference between the lattice constants of WSe_2 (3.28 Å) and WS_2 (3.15 Å). These results are similar to the moiré pattern previously observed in a WSe_2/MoS_2 vertical heterostructure.[35,36]

To obtain further insight into the moiré pattern, STS was performed. Figure 4d is the color scale map of dI/dV at V_s = −1.8 V reflecting change of the valence band LDOS corresponding to the moiré pattern. We note that the LDOS of the conduction band hardly changed. Figure 4e exhibits the dI/dV curves of three different points in Figure 4d. In these curves, the threshold voltages at positive and negative voltages correspond to conduction band minimum (CBM) and valence band maximum (VBM). Depending on the position, only the VBM shifts by approximately 0.2 eV. The periodic change of the VBM can be clearly seen from color scale map based on dI/dV curves in Figure 4f. Because the VBM of multilayer TMDCs is located at the Γ point,[25] these results indicate that the interlayer interaction affects the Γ point of the valence

DOI: 10.1021/acsnano.8b07991
ACS Nano 2019, 13, 7527−7535

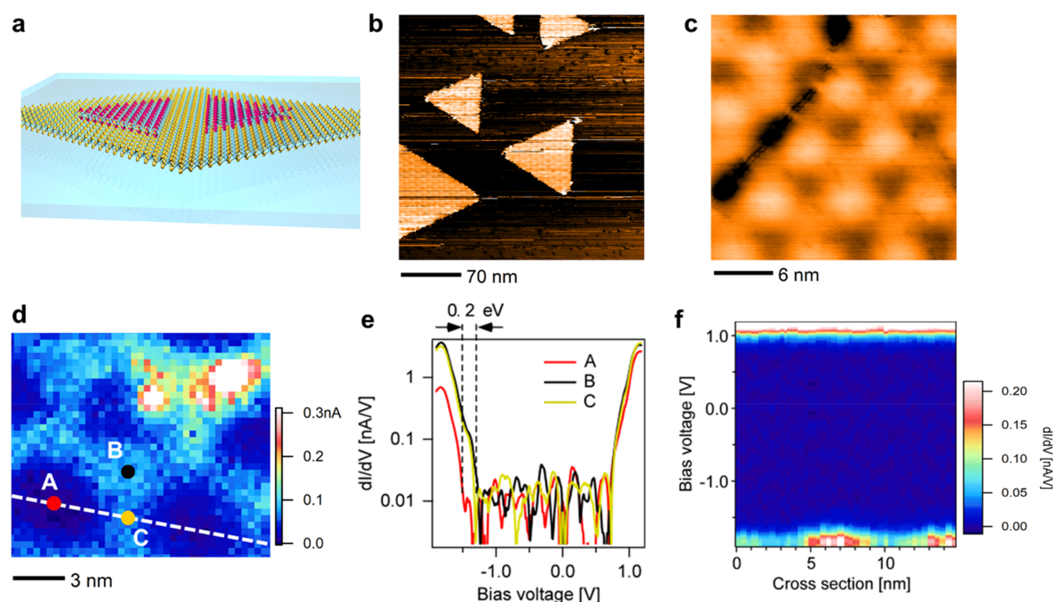

Figure 4. (a) Structural model and (b) wide-area (V_s = +1.5 V, I_t = 0.05 nA) and (c) magnified (V_s = +1.5 V, I_t = 0.1 nA) STM images of a WSe_2/WS_2 vertical heterostructure. (d) Color scale map of dI/dV at V_s = −1.80 V. (e) dI/dV curves of three different points (A, B, C) in (d). (f) Color scale map based on dI/dV curves calculated from the spatially resolved scanning tunneling spectroscopy (STS) spectra acquired along the white dotted line in (d).

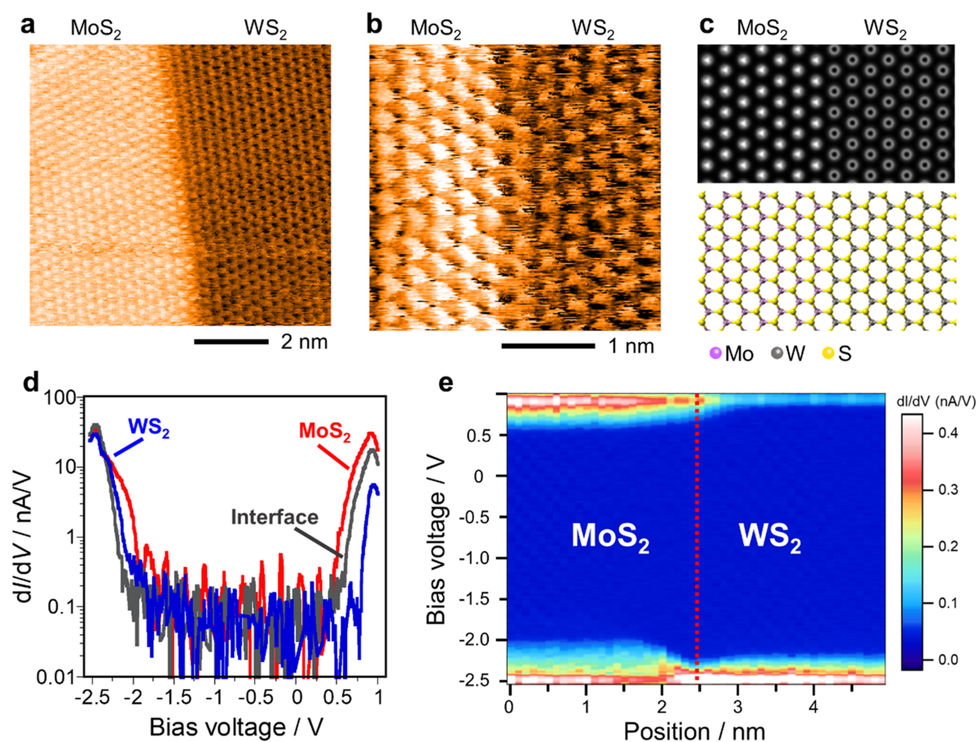

Figure 5. (a and b) STM images (V_s = +1.0 V, I_t = 0.08 nA) and (c) a spatial map of the calculated total LDOS (top) and structural model (bottom) of the MoS_2/WS_2 heterointerface. The total LDOS was obtained by the integration of the DOS within the energy range from E_F to E_F + 3 eV. (d) Averaged dI/dV spectra obtained from the MoS_2, WS_2 and heterointerface regions. (e) Color scale map of the dI/dV spectra measured in the vicinity of the heterointerface. In (e), the red dotted line indicates the position of MoS_2/WS_2 heterointerface.

band and formation of an electronic superlattice corresponding to the moiré pattern.[35−37]

To investigate the interface structures, atomically resolved images of the interfaces of in-plane MoS_2/WS_2 monolayer heterostructures were obtained by high-resolution STM, as shown in Figures 5a,b and S4. In these images, the left and right sides correspond to MoS_2 and WS_2, respectively, and Mo (W) atoms can be seen as bright (dark) dots under the present measurement conditions, due to the difference in LDOS between the two.[15,34] The STM images are in good agreement with a spatial map of the total LDOS obtained by first-principles calculations (Figure 5c). In this sample, the WS_2 was grown from the edge of the MoS_2, and it is noteworthy that the Mo and W atoms were perfectly separated along the

DOI: 10.1021/acsnano.8b07991
ACS Nano 2019, 13, 7527−7535

heterointerface. Furthermore, the STM images demonstrate that the heterointerface junction consisted of atomically straight zigzag edges of Mo and W atoms and that the MoS_2 and WS_2 honeycomb lattices were smoothly connected with one another. From these results, it is apparent that the present process enabled heteroepitaxial growth initiated at the edges of the first-growth grains. We note that the formation of atomically sharp interface and the isotropic growth of individual triangle-shaped grains during heteroepitaxy (Figure 2) indicate that individual metals and chalcogens are decomposed from the metal−organic precursors and then are adsorbed on the edge while diffusing. In other words, the vapor−solid−solid (VSS) mechanism plays a major role in the present epitaxial growth rather than the vapor−liquid−solid mechanism as observed in recent salt-assisted CVD.[38]

In previous studies, the interfaces tended to have disordered structures, likely due to the low degree of crystallinity as well as degradation during the second growth process, partly as a result of exposure to air.[16,18,19,37] In the case of the technique reported herein, a high-quality interface was possible because the process was continuous, proceeded without exposure to air, and exposed the liquid precursors to a relatively low growth temperature. It should be noted that optimization of precursor supply rates and growth temperature for each TMDC was also necessary to obtain atomically straight edges. The formation of atomically straight interface can be explained by the following reasons. First, the suppression of kink formation could be achieved by smaller thermal fluctuation under low temperature growth. Low temperature growth is enabled by the present liquid precursors, which are easily decomposed at lower temperature compared with solid precursors. Additionally, the continuous growth without air exposure of samples can avoid the adsorption of impurities and oxidation at reactive grain edges. The controlled supply rates of liquid precursors would be also important to improve uniformity of edge structures. We note that a similar advantage is expected for the metal−organic precursors used in the previous works.[22,23,31] A major difference between the present liquid precursors and the well-used organic precursors such as $Mo(CO)_6$ and $W(CO)_6$ is the presence of oxygen atoms, which may influence the quality and grain size of samples. For the heterostructures with different chalcogen atoms such as $MoS_2/MoSe_2$, both MoS_2 and $MoSe_2$ tend to alloy around the heterointerfaces probably due to the chalcogen substitution and migration during growth, as observed in our STM result (Figure S5). To fabricate an atomically straight interface of the heterostructures with different chalcogen atoms, it would be necessary to conduct the growth at a lower temperature.

The spatial variations in the LDOS of MoS_2/WS_2 and $MoS_2/MoSe_2$ monolayer heterointerfaces were investigated by STS analyses. Figure S6a presents the spectra obtained from averaged dI/dV values (where I and V are the tunneling current and bias voltage, respectively) for the MoS_2, WS_2, and heterointerface regions. Based on the threshold voltages for the dI/dV values, the MoS_2 and WS_2 bandgaps were estimated to be 2.2 and 2.4 eV, respectively, both of which are consistent with previous reports (2.2 eV for MoS_2 and 2.4 eV for WS_2 at room temperature,[39] 2.4 eV for MoS_2 at 77 K[40]). The difference of bandgaps could result from the presence of lattice strain in the in-plane heterostructures at 83 K, which can be introduced by a mismatch in the lattice constants and/or thermal expansion coefficients.[41−43] The valence and conduction band edges were smoothly connected within the 2−3 nm zone around the interface, as shown in the color scale map of the dI/dV spectra (Figure S6b). The CBM and VBM of the MoS_2 monolayer were located below the CBM and VBM of the WS_2 monolayer, respectively, indicating the formation of a type II staggered gap at the heterointerface. A similar type II staggered gap is observed for the $MoS_2/MoSe_2$ heterojunction (Figure S5b,c). Interestingly, at a different grain, the CBM and VBM of the MoS_2 were located within the bandgap of the WS_2, indicating that the interface has a type I straddling gap as shown in Figure 5d,e, and the bandgaps are also changed to be 2.1 eV for the MoS_2 and 2.5 eV for WS_2. The LDOS of MoS_2/WS_2 was uniform at least within the scanning area (around 6 nm × 6 nm) along the interface (Figure S7). This modulation of band structure is probably caused by grain-dependent lattice strain. The grain-dependent strain is actually found in the PL spectra. As shown in Figure S8, the PL peak positions of MoS_2 and WS_2 at the WS_2/MoS_2 interfaces are shifted in different triangle-shaped grains and even within the identical grain. The peak positions of MoS_2 varies more than these of WS_2. The variations suggest that the lattice strain depends on the size of MoS_2 and WS_2 in individual grains. In other words, these results suggest that the band alignment of the MoS_2/WS_2 in-plane heterostructure can be tuned by applying lattice strain. The strain-induced conversion from type II to type I band alignment was also observed for the WSe_2/MoS_2 heterostructure by STM/STS measurements.[36] In the case of WSe_2/MoS_2, the bandgap of MoS_2 is reduced by approximately 0.5 eV due to large strain induced by the lattice mismatch between MoS_2 and WSe_2. Our results provide additional evidence that, even for the WS_2/MoS_2 in-plane heterostructure, the lattice strain affects the band alignment at the interface.

These experimental results were subsequently compared with the calculated LDOC and band diagram for the MoS_2/WS_2 interface (Figure S6c,d). The calculated bandgaps of MoS_2 and WS_2 were 1.8 eV . The associated band edges were smoothly shifted within a region of 1 nm around the interface, and the MoS_2 was found to have lower CBM and VBM than the WS_2. This theoretical result suggests that the MoS_2/WS_2 heterointerface intrinsically has the type II band alignment, and the formation of type I band alignment (Figure 5d,e) could be derived from the strain effect. We note that the type II staggered gap coincides with the band alignment in MoS_2/WS_2 vertical heterostructures.[39]

The presence of strain effect is also supported by a small dip in the experimental VBM data in the vicinity of the interface (Figure 5d,e). This phenomenon can possibly be attributed to the presence of a positive fixed charge, likely resulting from the piezoelectric effect induced by lattice strain at the interface, as discussed in our previous report.[15] This potential modulation of the interface could have applications to the switching of electronic transport across the interface as well as carrier accumulation along the interface.

CONCLUSIONS

In summary, we have demonstrated the continuous heteroepitaxial growth of various 2D heterostructures with atomically straight heterointerfaces by switching between liquid precursors. The present liquid precursors enable a continuously and controllable supply and the growth of high-quality specimens even at a relatively low temperature of 640 °C, as recently demonstrated by other metal organic precursors.[23] Our study provides another choice for the growth of TMDC-based heterostructures. This technique also allowed us to

DOI: 10.1021/acsnano.8b07991
ACS Nano 2019, 13, 7527−7535

demonstrate the formation of MoS_2 nanoribbons with a width of 20 nm via epitaxial growth from the edges of TMDC monolayers, as well as vertical heterostructures. The present process has several advantages as follows. We have achieved a direct growth of samples on graphite, which facilitates the STM/STS study without the need for wet or dry transfer. We found that the heterointerfaces exhibit perfect zigzag edges without alloying and revealed the LDOS of both the lateral and the vertical heterostructures. The obtained band diagram of MoS_2/WS_2 in-plane heterostructure was compared with the results of first-principles calculations. This work suggests a means of fabricating a wide variety of in-plane and vertical superlattices, nanoribbons, and nanowires.

EXPERIMENTAL METHODS

In this work, four liquid precursors were employed during MOCVD growth: $(t\text{-BuN}{=})_2W(NMe_2)_2$, $(t\text{-BuN}{=})_2Mo(NMe_2)_2$, $(t\text{-}C_4H_9)_2S_2$, and $(C_2H_5)_2Se_2$ (Gas-Phase Growth, Ltd.). TMDC crystals were grown on either SiO_2/Si or Kish graphite flakes (Type B, Covalent Materials Co.), as reported previously.[33] The substrates were placed in a quartz tube (3 cm diameter, 70 cm long) with NaCl (100 mg, Wako Pure Chemical Industries, Ltd.), after which the tube was filled with a N_2/H_2 gas mixture at a flow rate of 594/6 cm^3/min. NaCl powder was palced at 1−3 cm upstream of substrates, and its temperature is around 540−590 °C. The temperature of the substrate was gradually increased to the growth temperature (590 to 640 °C) over 20 min using an electric furnace. When the substrate temperature was at the set point, the precursors were supplied by bubbling N_2 through precursor reservoirs to the substrate for 60 min under atmospheric pressure. During this step, the liquid precursors were kept at room temperature (24 to 25 °C). The growth conditions used to obtain MoS_2, WS_2, WSe_2, and $MoSe_2$ monolayers are summarized in Table S1. Following this growth process, the quartz tube was immediately cooled using an electric fan.

In-plane heterostructures and nanoribbon structures were obtained by conducting a second MOCVD immediately after the first growth, without cooling the furnace. The quartz tube was filled with N_2/H_2 gas at a flow rate of 594/6 cm^3/min for 2 min at the desired growth temperature (when making MoS_2/WS_2, WSe_2/WS_2, $MoS_2/MoSe_2$, and $WSe_2/MoSe_2$) or for 30 min at room temperature (when making $WS_2/MoSe_2$ and MoS_2/WSe_2) to remove residual precursor from the first growth. To keep the room temperature, the furnace was moved during removal of residual precursor. The second TMDC growth was then conducted in the same manner as the first over a span of 30 min. The multiheterostructures were prepared by an initial WS_2 growth step over 60 min, a second MoS_2 growth over 30 min, and a third WS_2 growth over 30 min.

For the growth of vertical heterostructures, the quartz tube was filled with N_2/H_2 gas at a flow rate of 594/6 cm^3/min for 30 min at room temperature after the growth of a WS_2 monolayer on graphite. WSe_2 growth was then conducted in the same manner as the first growth over 30 min.

Samples were observed using optical microscopy (Nikon, Eclipse-LV100D). Raman and PL spectra and PL intensity maps were acquired using a micro-Raman spectroscope (Renishaw, in*Via*) with a 532 nm excitation laser. STM/STS assessments were carried out using a low-temperature STM system (Omicron, LT-STM) operating at 83 K.

All calculations were based on the density functional theory (DFT)[44,45] and implemented using the STATE software package.[46] We employed the generalized gradient approximation[47] and ultrasoft pseudopotentials[48] to describe the exchange-correlation potential and the electron−ion interaction, respectively. The valence wave functions and deficit charge density were expanded in conjunction with a plane-wave basis set, applying cutoff energies of 25 and 225 Ryd, respectively. The Brillouin zone integration was performed with a $1 \times 16 \times 1$ uniform k-point grid. To simulate the border between WS_2 and MoS_2, we constructed a superlattice consisting of WS_2 and MoS_2 strips with widths of 10 zigzag chains of MoS_2 and WS_2 molecules in an alternating arrangement. The unit cell used in these calculations is shown in Figure S9. In this model, the TMDC heterosheet was separated from its periodic images by a 0.89 nm vacuum space. The geometric structure of the heterosheet was optimized based on the experimental lattice constant of MoS_2 until the remaining force acting on the atoms was less than 0.005 Ryd/Å.

ASSOCIATED CONTENT

Supporting Information

The Supporting Information is available free of charge on the ACS Publications website at DOI: 10.1021/acsnano.8b07991.

> Table of growth parameters for WS_2, WSe_2, MoS_2, and $MoSe_2$ monolayers in the present study (Table S1); optical microscopy images of WS_2 grown on SiO_2/Si via MOCVD with and without NaCl (Figure S1); optical microscopy images of $MoSe_2$ grown with different supply rates for the metal and chalcogen precursors (Figure S2); optical image, PL intensity maps, and Raman spectra of MoS_2/WS_2, WSe_2/WS_2, $MoS_2/MoSe_2$, $WSe_2/MoSe_2$, $WS_2/MoSe_2$, and MoS_2/WSe_2 heterostructure (Figure S3); STM images of the MoS_2/WS_2 heterointerface from different regions (Figure S4); STM image and color scale map of the d*I*/d*V* spectra acquired in the vicinity of the heterointerface and averaged d*I*/d*V* spectra obtained from the $MoS_2/MoSe_2$ heterostructure (Figure S5); averaged d*I*/d*V* spectra, color scale map of the d*I*/d*V* spectra acquired in the vicinity of the heterointerface, calculated LDOS, and associated color scale map for the MoS_2/WS_2 heterostructure (Figure S6); STM image and d*I*/d*V* map of the area around the MoS_2/WS_2 heterointerface (Figure S7); PL spectra and peak position plot of MoS_2 and WS_2 at the WS_2/MoS_2 interfaces in different triangle-shaped grains and within the same grain (Figure S8); and unit cell of a superlattice consisting of WS_2 and MoS_2 strips used for theoretical calculations (Figure S9) (PDF)

AUTHOR INFORMATION

Corresponding Author

*(Y. Miyata) E-mail: ymiyata@tmu.ac.jp.

ORCID

Yu Kobayashi: 0000-0001-8305-0991
Hidemi Shigekawa: 0000-0001-9550-5148
Yasumitsu Miyata: 0000-0002-9733-5119

Author Contributions

Y.K. prepared all experimental samples and performed the optical analyses. S.Y., H.M., and K.M. carried out the STM/STS observations, with H.M. and O.T. providing technical assistance. M.M. and S.O. performed the theoretical calculations. Y.Miyata developed the concept and supervised the project. Y.K., S.Y., M.M., S.O., and Y.Miyata prepared the figures and wrote the paper. All authors discussed the results and commented on the manuscript.

Notes

The authors declare no competing financial interest.

ACKNOWLEDGMENTS

This work was supported by a JST CREST grant (number JPMJCR16F3) and by JSPS KAKENHI grants (numbers JP18H01832, JP17H06088, JP15H05412, and JP16H00918).

REFERENCES

(1) Esaki, L.; Howard, W. E.; Heer, J. The Interface Transport Properties of Ge-GaAs Heterojunctions. *Surf. Sci.* **1964**, *2*, 127−135.
(2) Hayashi, I.; Panish, M. B. GaAs-$Ga_xAl_{1-x}As$ Heterostructure Injection Lasers which Exhibit Low Thresholds at Room Temperature. *J. Appl. Phys.* **1970**, *41*, 150−163.
(3) Nakamura, S.; Senoh, M.; Nagahama, S.-i.; Iwasa, N.; Yamada, T.; Matsushita, T.; Kiyoku, H.; Sugimoto, Y. InGaN-Based Multi-Quantum-Well-Structure Laser Diodes. *Jpn. J. Appl. Phys.* **1996**, *35*, L74.
(4) Faist, J.; Capasso, F.; Sivco, D. L.; Sirtori, C.; Hutchinson, A. L.; Cho, A. Y. Quantum Cascade Laser. *Science* **1994**, *264*, 553.
(5) Esaki, L.; Tsu, R. Superlattice and Negative Differential Conductivity in Semiconductors. *IBM J. Res. Dev.* **1970**, *14*, 61−65.
(6) Dingle, R.; Störmer, H. L.; Gossard, A. C.; Wiegmann, W. Electron Mobilities in Modulation-Doped Semiconductor Heterojunction Superlattices. *Appl. Phys. Lett.* **1978**, *33*, 665−667.
(7) Mimura, T.; Hiyamizu, S.; Fujii, T.; Nanbu, K. A New Field-Effect Transistor with Selectively Doped GaAs/n-$Al_xGa_{1-x}As$ Heterojunctions. *Jpn. J. Appl. Phys.* **1980**, *19*, L225.
(8) Störmer, H. L.; Dingle, R.; Gossard, A. C.; Wiegmann, W.; Sturge, M. D. Two-Dimensional Electron Gas at a Semiconductor-Semiconductor Interface. *Solid State Commun.* **1979**, *29*, 705−709.
(9) Tsui, D. C.; Stormer, H. L.; Gossard, A. C. Two-Dimensional Magnetotransport in the Extreme Quantum Limit. *Phys. Rev. Lett.* **1982**, *48*, 1559−1562.
(10) Störmer, H. L.; Tsui, D. C.; Gossard, A. C. The Fractional Quantum Hall Effect. *Rev. Mod. Phys.* **1999**, *71*, S298−S305.
(11) Levendorf, M. P.; Kim, C.-J.; Brown, L.; Huang, P. Y.; Havener, R. W.; Muller, D. A.; Park, J. Graphene and Boron Nitride Lateral Heterostructures for Atomically Thin Circuitry. *Nature* **2012**, *488*, 627.
(12) Sutter, P.; Cortes, R.; Lahiri, J.; Sutter, E. Interface Formation in Monolayer Graphene-Boron Nitride Heterostructures. *Nano Lett.* **2012**, *12*, 4869−4874.
(13) Miyata, Y.; Maeda, E.; Kamon, K.; Kitaura, R.; Sasaki, Y.; Suzuki, S.; Shinohara, H. Fabrication and Characterization of Graphene/Hexagonal Boron Nitride Hybrid Sheets. *Appl. Phys. Express* **2012**, *5*, 085102.
(14) Kobayashi, Y.; Mori, S.; Maniwa, Y.; Miyata, Y. Bandgap-Tunable Lateral and Vertical Heterostructures Based on Monolayer $Mo_{1-x}W_xS_2$ Alloys. *Nano Res.* **2015**, *8*, 3261−3271.
(15) Kobayashi, Y.; Yoshida, S.; Sakurada, R.; Takashima, K.; Yamamoto, T.; Saito, T.; Konabe, S.; Taniguchi, T.; Watanabe, K.; Maniwa, Y.; Takeuchi, O.; Shigekawa, H.; Miyata, Y. Modulation of Electrical Potential and Conductivity in an Atomic-Layer Semiconductor Heterojunction. *Sci. Rep.* **2016**, *6*, 31223.
(16) Li, M.-Y.; Shi, Y.; Cheng, C.-C.; Lu, L.-S.; Lin, Y.-C.; Tang, H.-L.; Tsai, M.-L.; Chu, C.-W.; Wei, K.-H.; He, J.-H.; Chang, W.-H.; Suenaga, K.; Li, L.-J. Epitaxial Growth of a Monolayer WSe_2-MoS_2 Lateral *p-n* Junction with an Atomically Sharp Interface. *Science* **2015**, *349*, 524.
(17) Gong, Y.; Lin, J.; Wang, X.; Shi, G.; Lei, S.; Lin, Z.; Zou, X.; Ye, G.; Vajtai, R.; Yakobson, B. I.; Terrones, H.; Terrones, M.; Tay, B. K.; Lou, J.; Pantelides, S. T.; Liu, Z.; Zhou, W.; Ajayan, P. M. Vertical and In-Plane Heterostructures from WS_2/MoS_2 Monolayers. *Nat. Mater.* **2014**, *13*, 1135.
(18) Duan, X.; Wang, C.; Shaw, J. C.; Cheng, R.; Chen, Y.; Li, H.; Wu, X.; Tang, Y.; Zhang, Q.; Pan, A.; Jiang, J.; Yu, R.; Huang, Y.; Duan, X. Lateral Epitaxial Growth of Two-Dimensional Layered Semiconductor Heterojunctions. *Nat. Nanotechnol.* **2014**, *9*, 1024.
(19) Huang, C.; Wu, S.; Sanchez, A. M.; Peters, J. J. P.; Beanland, R.; Ross, J. S.; Rivera, P.; Yao, W.; Cobden, D. H.; Xu, X. Lateral Heterojunctions within Monolayer $MoSe_2/WSe_2$ Semiconductors. *Nat. Mater.* **2014**, *13*, 1096.
(20) Zhang, Z.; Chen, P.; Duan, X.; Zang, K.; Luo, J.; Duan, X. Robust Epitaxial Growth of Two-Dimensional Heterostructures, Multiheterostructures, and Superlattices. *Science* **2017**, *357*, 788−792.
(21) Sahoo, P. K.; Memaran, S.; Xin, Y.; Balicas, L.; Gutiérrez, H. R. One-Pot Growth of Two-Dimensional Lateral Heterostructures *via* Sequential Edge-Epitaxy. *Nature* **2018**, *553*, 63.
(22) Kang, K.; Xie, S.; Huang, L.; Han, Y.; Huang, P. Y.; Mak, K. F.; Kim, C.-J.; Muller, D.; Park, J. High-Mobility Three-Atom-Thick Semiconducting Films with Wafer-Scale Homogeneity. *Nature* **2015**, *520*, 656.
(23) Xie, S.; Tu, L.; Han, Y.; Huang, L.; Kang, K.; Lao, K. U.; Poddar, P.; Park, C.; Muller, D. A.; DiStasio, R. A.; Park, J. Coherent, Atomically Thin Transition-Metal Dichalcogenide Superlattices with Engineered Strain. *Science* **2018**, *359*, 1131−1136.
(24) Wang, Q. H.; Kalantar-Zadeh, K.; Kis, A.; Coleman, J. N.; Strano, M. S. Electronics and Optoelectronics of Two-Dimensional Transition Metal Dichalcogenides. *Nat. Nanotechnol.* **2012**, *7*, 699.
(25) Chhowalla, M.; Shin, H. S.; Eda, G.; Li, L.-J.; Loh, K. P.; Zhang, H. The Chemistry of Two-Dimensional Layered Transition Metal Dichalcogenide Nanosheets. *Nat. Chem.* **2013**, *5*, 263.
(26) Zhang, Y. J.; Oka, T.; Suzuki, R.; Ye, J. T.; Iwasa, Y. Electrically Switchable Chiral Light-Emitting Transistor. *Science* **2014**, *344*, 725.
(27) Zeng, H.; Dai, J.; Yao, W.; Xiao, D.; Cui, X. Valley Polarization in MoS_2 Monolayers by Optical Pumping. *Nat. Nanotechnol.* **2012**, *7*, 490.
(28) Mak, K. F.; He, K.; Shan, J.; Heinz, T. F. Control of Valley Polarization in Monolayer MoS_2 by Optical Helicity. *Nat. Nanotechnol.* **2012**, *7*, 494.
(29) van der Zande, A. M.; Huang, P. Y.; Chenet, D. A.; Berkelbach, T. C.; You, Y.; Lee, G.-H.; Heinz, T. F.; Reichman, D. R.; Muller, D. A.; Hone, J. C. Grains and Grain Boundaries in Highly Crystalline Monolayer Molybdenum Disulphide. *Nat. Mater.* **2013**, *12*, 554.
(30) Li, S.; Wang, S.; Tang, D.-M.; Zhao, W.; Xu, H.; Chu, L.; Bando, Y.; Golberg, D.; Eda, G. Halide-Assisted Atmospheric Pressure Growth of Large WSe_2 and WS_2 Monolayer Crystals. *Appl. Mater. Today* **2015**, *1*, 60−66.
(31) Kim, H.; Ovchinnikov, D.; Deiana, D.; Unuchek, D.; Kis, A. Suppressing Nucleation in Metal-Organic Chemical Vapor Deposition of MoS_2 Monolayers by Alkali Metal Halides. *Nano Lett.* **2017**, *17*, 5056−5063.
(32) Zhou, J.; Lin, J.; Huang, X.; Zhou, Y.; Chen, Y.; Xia, J.; Wang, H.; Xie, Y.; Yu, H.; Lei, J.; Wu, D.; Liu, F.; Fu, Q.; Zeng, Q.; Hsu, C.-H.; Yang, C.; Lu, L.; Yu, T.; Shen, Z.; Lin, H.; et al. A Library of Atomically Thin Metal Chalcogenides. *Nature* **2018**, *556*, 355−359.
(33) Kobayashi, Y.; Sasaki, S.; Mori, S.; Hibino, H.; Liu, Z.; Watanabe, K.; Taniguchi, T.; Suenaga, K.; Maniwa, Y.; Miyata, Y. Growth and Optical Properties of High-Quality Monolayer WS_2 on Graphite. *ACS Nano* **2015**, *9*, 4056−4063.
(34) Yoshida, S.; Kobayashi, Y.; Sakurada, R.; Mori, S.; Miyata, Y.; Mogi, H.; Koyama, T.; Takeuchi, O.; Shigekawa, H. Microscopic Basis for the Band Engineering of $Mo_{1-x}W_xS_2$-Based Heterojunction. *Sci. Rep.* **2015**, *5*, 14808.
(35) Pan, Y.; Fölsch, S.; Nie, Y.; Waters, D.; Lin, Y.-C.; Jariwala, B.; Zhang, K.; Cho, K.; Robinson, J. A.; Feenstra, R. M. Quantum-Confined Electronic States Arising from the Moiré Pattern of MoS_2-WSe_2 Heterobilayers. *Nano Lett.* **2018**, *18*, 1849−1855.
(36) Zhang, C.; Li, M.-Y.; Tersoff, J.; Han, Y.; Su, Y.; Li, L.-J.; Muller, D. A.; Shih, C.-K. Strain Distributions and Their Influence on Electronic Structures of WSe_2-MoS_2 Laterally Strained Heterojunctions. *Nat. Nanotechnol.* **2018**, *13*, 152−158.
(37) Zhang, C.; Chuu, C.-P.; Ren, X.; Li, M.-Y.; Li, L.-J.; Jin, C.; Chou, M.-Y.; Shih, C.-K. Interlayer Couplings, Moiré Patterns, and 2D Electronic Superlattices in MoS_2/WSe_2 Hetero-Bilayers. *Sci. Adv.* **2017**, *3*, No. e1601459.
(38) Li, S.; Lin, Y.-C.; Zhao, W.; Wu, J.; Wang, Z.; Hu, Z.; Shen, Y.; Tang, D.-M.; Wang, J.; Zhang, Q.; Zhu, H.; Chu, L.; Zhao, W.; Liu, C.; Sun, Z.; Taniguchi, T.; Osada, M.; Chen, W.; Xu, Q.-H.; Wee, A. T. S.; et al. Vapour-Liquid-Solid Growth of Monolayer MoS_2 Nanoribbons. *Nat. Mater.* **2018**, *17*, 535−542.
(39) Hill, H. M.; Rigosi, A. F.; Rim, K. T.; Flynn, G. W.; Heinz, T. F. Band Alignment in MoS_2/WS_2 Transition Metal Dichalcogenide

DOI: 10.1021/acsnano.8b07991
ACS Nano 2019, 13, 7527−7535

Heterostructures Probed by Scanning Tunneling Microscopy and Spectroscopy. *Nano Lett.* **2016**, *16*, 4831−4837.

(40) Huang, Y. L.; Chen, Y.; Zhang, W.; Quek, S. Y.; Chen, C.-H.; Li, L.-J.; Hsu, W.-T.; Chang, W.-H.; Zheng, Y. J.; Chen, W.; Wee, A. T. S. Bandgap Tunability at Single-Layer Molybdenum Disulphide Grain Boundaries. *Nat. Commun.* **2015**, *6*, 6298.

(41) Zhu, Z. Y.; Cheng, Y. C.; Schwingenschlögl, U. Giant Spin-Orbit-Induced Spin Splitting in Two-Dimensional Transition-Metal Dichalcogenide Semiconductors. *Phys. Rev. B: Condens. Matter Mater. Phys.* **2011**, *84*, 153402.

(42) Matthäus, A.; Ennaoui, A.; Fiechter, S.; Tiefenbacher, S.; Kiesewetter, T.; Diesner, K.; Sieber, I.; Jaegermann, W.; Tsirlina, T.; Tenne, R. Highly Textured Films of Layered Metal Disulfide 2H-WS_2: Preparation and Optoelectronic Properties. *J. Electrochem. Soc.* **1997**, *144*, 1013−1019.

(43) El-Mahalawy, S. H.; Evans, B. L. The Thermal Expansion of 2H-MoS_2, 2H-$MoSe_2$ and 2H-WSe_2 between 20 and 800 °C. *J. Appl. Crystallogr.* **1976**, *9*, 403−406.

(44) Hohenberg, P.; Kohn, W. Inhomogeneous Electron Gas. *Phys. Rev.* **1964**, *136*, B864−B871.

(45) Kohn, W.; Sham, L. J. Self-Consistent Equations Including Exchange and Correlation Effects. *Phys. Rev.* **1965**, *140*, A1133−A1138.

(46) Morikawa, Y.; Iwata, K.; Terakura, K. Theoretical Study of Hydrogenation Process of Formate on Clean and Zn Deposited Cu(111) Surfaces. *Appl. Surf. Sci.* **2001**, *169*−*170*, 11−15.

(47) Perdew, J. P.; Burke, K.; Ernzerhof, M. Generalized Gradient Approximation Made Simple. *Phys. Rev. Lett.* **1996**, *77*, 3865−3868.

(48) Vanderbilt, D. Soft Self-Consistent Pseudopotentials in a Generalized Eigenvalue Formalism. *Phys. Rev. B: Condens. Matter Mater. Phys.* **1990**, *41*, 7892−7895.

DOI: 10.1021/acsnano.8b07991
ACS Nano 2019, 13, 7527−7535